European Journal of Mechanics B/Fluids 55 (2016) 229–240

Contents lists available at ScienceDirect

European Journal of Mechanics B/Fluids

journal homepage: www.elsevier.com/locate/ejmflu

Effect of mesh resolution on large eddy simulation of cloud cavitating flow around a three dimensional twisted hydrofoil

X.C. Wu, Y.W. Wang *, C.G. Huang

Key Laboratory for Mechanics in Fluid Solid Coupling Systems, Institute of Mechanics, Chinese Academy of Sciences, Hai dian District No.15 Beisihuanxi Road, Beijing, China

HIGHLIGHTS

- Two sets of grids are used to investigate the influence of mesh resolution.
- The smaller grid spacing is needed to capture the details of re-entry jet.
- The re-entry jet is sensitive to the pressure gradient and spanwise mesh resolution.

ARTICLE INFO

Article history:
Received 30 March 2015
Received in revised form
13 August 2015
Accepted 27 September 2015
Available online 1 November 2015

Keywords:
Large eddy simulation
Twisted wing
Influence of mesh
Cavity length
Cavitation patterns

ABSTRACT

Unsteady cavitating turbulent flow around a twisted wing is simulated by using the large eddy simulation method. Two sets of grids with 10 million and 2 million nodes are used to investigate the influence of mesh resolution on the results. The results of non-cavitating flow with the coarse mesh agree well with the experiment, but the accuracy of the fine mesh results is remarkably higher for the cavitating flow, which indicates that more nodes are needed for the cavitating flow simulation than the non-cavitating flow. Then the parameters affecting the grid resolution are investigated. It is observed that the small size shedding vortex can only be captured by the fine mesh and the smaller grid spacing in the spanwise direction is needed to capture the details of re-entry jet. The re-entry jet in spanwise direction can affect the overall development of cavities, which is sensitive to the pressure gradient and spanwise resolution of the mesh.

1. Introduction

On account of blades and propellers on hydraulic machines have not only three-dimensional geometries but also non-uniform loading in the span-wise direction. Thus, the flow structure and three-dimensional effects on cavitating flow should be investigated. A series test of swept wedges was studied by Ceccio [1] to confirm the influence factor of cavity instability. Dular et al. [2] investigated the re-entrant jet reflection at an inclined cavity closure line around a hydrofoil with an asymmetric leading edge. De Lange and De Bruin [3] tested transparent hydrofoils in a cavitation water tunnel to show the flow characteristics with the re-entrant jet velocity component. Dang and Kuiper [4] calculated the steady 3D cavity flow on a hydrofoil surface, which confirmed that the flow on the cavity surface was reflected at the cavity end line when the re-entrant jet exists. Saito et al. [5] investigated cavitating flows around a three-dimensional hydrofoil with uniform profiles and uniform attack angles along the spanwise direction and found that the sidewall effect was the main reason for generation of the U-shaped cavitation. Schnerr et al. [6] demonstrated that collapse induced shocks generate high impulsive loads on the surface of a three-dimensional 3D hydrofoil. Unsteady cavitating flow computations for the 2D modified NACA66 and 3D twisted hydrofoils were carried out and compared with existing experimental data by Sunho Park [7]. Foeth et al. [8–10] numerically and experimentally studied the cavitating flow around the Delft twisted hydrofoil, and the flow structure was observed with a high-speed camera. An implicit pressure-based algorithm (IPA) had been developed for the computations of the two-phase cavitating flows by Zhang and Khoo [11].

The unsteady behavior of cavitating flows and cavity shedding is associated with the vortex motion. The turbulent solution approach is the key part in the numerical simulation to depict the cavitating flow structure. For a long time, Reynolds-averaged Navier–Stokes equations (RANS) with different turbulent model were solved for general engineering problems [12].

* Corresponding author. Tel.: +86 10 82543811; fax: +86 10 82543811.
E-mail address: wangyw@imech.ac.cn (Y.W. Wang).

http://dx.doi.org/10.1016/j.euromechflu.2015.09.011
0997-7546/

In general, turbulence models seek to modify the original unsteady Navier–Stokes equations by the introduction of averaged and fluctuating quantities to produce the Reynolds Averaged Navier–Stokes (RANS) equations. These equations represent the mean flow quantities only, while modeling turbulence effects without a need for the resolution of the turbulent fluctuations. So, the RANS models have limited capability to simulate unsteady cavitating flows and need some modifications [13–18]. The Large Eddy Simulation (LES) method can calculate the large-scale vortices by solving the instantaneous Navier–Stokes equations directly, while the impact of small-scale vortices is achieved with models [19]. Thus more refined resolutions of bubble and vortex structures can be obtained. LES method is expected to give better predictions of larger-scale turbulent eddies with better accuracy with some promising results already obtained. For example, an implicit LES method was used to simulate dynamic cavitation behavior of a propeller by Bensow et al. [20] and Lu et al. [21]. LES with the WALE SGS stress model was adopted to calculate the cavitation shedding and horse-shoe structures by Ji et al. [22–24] and Huang et al. [25]. A single fluid model of sheet/cloud cavitation was developed and applied to a NACA0015 hydrofoil by Wang [26]. The physical mechanism for the cavitation induced pressure fluctuations around a NACA66 hydrofoil was analyzed by Ji et al. [27]. The results of two different mass transfer models, namely Kunz and Sauer models, were compared with the experimental data for cavitation dynamics starting point of cavitation and force coefficients by Roohi et al. [28].

RANS with different turbulent model were solved for general engineering problems, but it cannot depict the cavitating flow structure of the unsteady cavitating flows exactly. Thus, LES method was adopted on cavitating flows in recent years, as a new kind of numerical method. Compared with RANS method, the influences of parameters (such as turbulent model, cavitation model, mesh setting and so on) are unclear in LES method. Especially the literature about the grid sensitivity of the results in cavitating flow is rare and needs more attentions, because the grid sensitivity in LES method for cavitating flow may be larger than that in RANS scheme for non-cavitating flow. Two set of grids are used to investigate the sensitivity of the grid resolution in this paper. Numerical simulations around a 3D twisted Delft hydrowing are carried out. The results of cavity shape evolutions are compared with the experimental results in detail. The characteristics such as vortices shedding, re-entry jets and pressure distributions are analyzed, in order to study the influences of mesh resolution on the cavitating flow simulations.

2. Numerical method

2.1. LES methods

The rationale behind the large-eddy simulation technique is a separation between large and small scales vortices. Filters are used to distinguish the vortex scales. If the vortex scales are smaller than a specified value in the filter, the vortex will be considered as a small-scale vortex and vice versa. The governing equations for LES are obtained by filtering the time-dependent Navier–Stokes equations in the physical space. The filtering process effectively filters out eddies whose scales are smaller than the filter width or grid spacing used in the computations. The resulting equations thus govern the dynamics of the large eddies [29]. In LES method, the large-scale vortices can be calculated by solving the instantaneous Navier–Stokes equations directly, while the impact of small-scale vortices is achieved with various cavitation models. The one equation subgrid-scale (SGS) model is adopted to consider the effect of small-scale vortices in this paper.

The basic governing equations consist of the mass and momentum conservation equations as follows:

$$\frac{\partial \rho}{\partial t} + \nabla \cdot (\rho \vec{v}) = 0 \tag{1}$$

$$\frac{\partial}{\partial t}(\rho \vec{v}) + \nabla \cdot (\rho \vec{v}\vec{v}) = -\nabla p + \nabla \cdot \mathbf{S} \tag{2}$$

where $\vec{v}$ is velocity, ρ is the density, p is the pressure, $\mathbf{S} = 2\mu\mathbf{D}$ is the viscous stress, μ is the dynamic viscosity coefficient, $\mathbf{D} = \frac{1}{2}\left(\nabla\vec{v} + \nabla\vec{v}^T\right)$ is fluid strain rate tensor.

In LES, ψ is decomposed into large-scale quantity $\bar{\psi}$ and small-scale quantity ψ'. $\bar{\psi}$ can be expressed as follows:

$$\bar{\psi} = \int_{-\infty}^{+\infty} \psi G\left(x, x'\right) dx' \tag{3}$$

where $\mathbf{G} = G\left(x, x'\right)$ is the filter function. In this paper, the widely used top-hat filter function is adopted,

$$G\left(x, x'\right) = \begin{cases} 1/\bar{\Delta} & \left|x - x'\right| \le \bar{\Delta}/2 \\ 0 & \left|x - x'\right| > \bar{\Delta}/2 \end{cases} \tag{4}$$

where $\bar{\Delta} = \sqrt[3]{\Delta_x \Delta_y \Delta_z}$ is the spatial filter size. Δ_x, Δ_y, Δ_z are the size of the grid in three directions.

By applying the above filter function to Eqs. (1) and (2), the LES equations are derived as

$$\frac{\partial \rho}{\partial t} + \nabla \cdot \left(\rho \bar{\vec{v}}\right) = 0 \tag{5}$$

$$\frac{\partial}{\partial t}\left(\rho \bar{\vec{v}}\right) + \nabla \cdot (\rho \overline{\vec{v}\vec{v}}) = -\nabla \bar{p} + \nabla \cdot (\bar{\mathbf{S}} - \mathbf{B}) \tag{6}$$

where the over-bars denote filtered quantities. $\bar{\mathbf{S}} = 2\mu\overline{\mathbf{D}}$ is the filtered viscous stress tensor. $\overline{\mathbf{D}} = 1/2\left(\nabla\bar{v} + \nabla\bar{v}^T\right)$ stands for the filtered rate of stress tensor. μ is the dynamic viscosity. $\mathbf{B} = \rho\left(\overline{\vec{v}\vec{v}} - \overline{\vec{v}}\,\overline{\vec{v}}\right)$ means the subgrid stress tensor, representing the influence of the small, unresolved eddies on the larger, resolved ones.

Based on Boussinesq hypothesis, a subgrid viscosity μ_{SGS} is considered. The resulting term in the LES equations becomes $\mathbf{B} = -2\mu_{SGS}\overline{\mathbf{D}}$. So that the whole viscous term can be described as a function of the effective viscosity μ_{eff} (summation of SGS turbulent viscosity μ_{SGS} and dynamic viscosity coefficient μ) and rate of stress tensor $\overline{\mathbf{D}}$, i.e., $\left(\bar{\mathbf{S}} - \mathbf{B}\right) = 2\mu_{\text{eff}}\overline{\mathbf{D}} = 2\left(\mu + \mu_{SGS}\right)\overline{\mathbf{D}}$, where μ_{SGS} needs to be solved.

In the present paper, the $k - \mu$ model is chosen to calculate the μ_{SGS}, and in this model the transport equation of SGS turbulent kinetic energy is included [30].

$$\frac{\partial k_{SGS}}{\partial t} + \nabla \cdot (k_{SGS}\overline{\mathbf{v}}) = \nabla \cdot \left[\left(\mu + \mu_{SGS}\right)\nabla k_{SGS}\right] + 2\mu_{SGS}\overline{\mathbf{D}}\overline{\mathbf{D}} - C_e \frac{k_{SGS}^{\frac{3}{2}}}{\Delta}. \tag{7}$$

Then, the SGS turbulent viscosity is obtained as $\mu_{SGS} = C_k \Delta \sqrt{k_{SGS}}$, where Δ is the filtered length for the SGS, which is the cube root of the grid volume. C_e and C_k are the constant, $C_e = 1.048$, $C_k = 0.094$.

2.2. Multiphase and cavitation modeling

VOF model is used to consider the interaction between water and vapor phases in the natural cavitation flow. The VOF model can model two or more immiscible fluids by solving a single set of momentum equations and tracking the volume fraction of each of

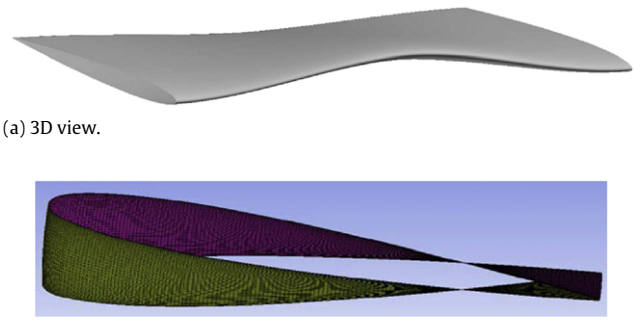

(a) 3D view.

(b) Side view.

Fig. 1. 3D twisted hydrofoil.

the fluids throughout the domain [31]. The density and viscosity of mixture can be expressed by the water volume fraction α,

$$\rho = \alpha\rho_l + (1-\alpha)\,\rho_v \tag{8}$$

$$\mu = \alpha\mu_l + (1-\alpha)\,\mu_v \tag{9}$$

where the subscript l denotes water, v denotes vapor.

A transport equation for the volume fraction needs to be incorporated into the filtered equations of continuity and momentum, Eqs. (5) and (6).

$$\frac{\partial\alpha}{\partial t} + \nabla\cdot(\bar{\vec{v}}\alpha) = \frac{\dot{m}}{\rho_v} \tag{10}$$

$$\nabla\cdot\bar{\vec{v}} = S_P \tag{11}$$

$$\frac{\partial}{\partial t}\left(\rho\bar{\vec{v}}\right) + \nabla\cdot(\rho\bar{\vec{v}}\bar{\vec{v}}) = -\nabla\bar{p} + \nabla\cdot(\bar{\mathbf{S}} - \mathbf{B}) \tag{12}$$

where $S_p = \left(\frac{1}{\rho_l} - \frac{1}{\rho_v}\right)\dot{m}$ is the source terms caused by phase change. $\dot{m}$ represents the mass transfer rate of evaporation and condensation, which is calculated by the Kunz cavitation model [32]. The model is based on two different strategies, as compared with most similar models that only rely on a single strategy for both creation and destruction of vapor. The vaporization $\dot{m}^+$ is formulated to be proportional to the amount by which pressure is below the vaporization pressure, and the condensation $\dot{m}^-$ is based on a third order polynomial function of the vapor volume fraction α_v:

$$\dot{m}^+ = \left(C_{prod}/U_\infty^2 t_\infty\right)\rho_v/\rho_l\cdot(1-\alpha_v)\min\left[0, \bar{p} - p_v\right] \tag{13}$$

$$\dot{m}^- = (C_{dest}/t_\infty)\,\rho_v(1-\alpha_v)^2\alpha_v \tag{14}$$

where the specific mass transfer rate is computed as $\dot{m} = \dot{m}^+ + \dot{m}^-$, and $C_{prod} = 10\,000$, $C_{dest} = 1000$, $U_\infty = 6.97$ m/s and $t_\infty = 0.02$ s.

2.3. Computational model and mesh

The Delft Twist-11 hydrofoil (as shown in Fig. 1) was used in the present paper. Relative experiments are performed in the Delft University Cavitation Tunnel. The experimental results concerning data on cavitation and flow properties of Delft Twist-11 hydrofoils are reported by Foeth et al. [10]. The chord length of the foil is 0.15 m and the span length is 0.3 m. The hydrofoil consists of a NACA0009 profile that has a spanwise varying attack angle from 0° at the tunnel walls to 11° at the mid-section. The hydrofoil is symmetry with its midspan plane. The attack angle of the entire hydrofoil is −2°.

The cavitation number is defined as

$$\sigma = \frac{p_{out} - p_v}{0.5\rho_l V_\infty^2} \tag{15}$$

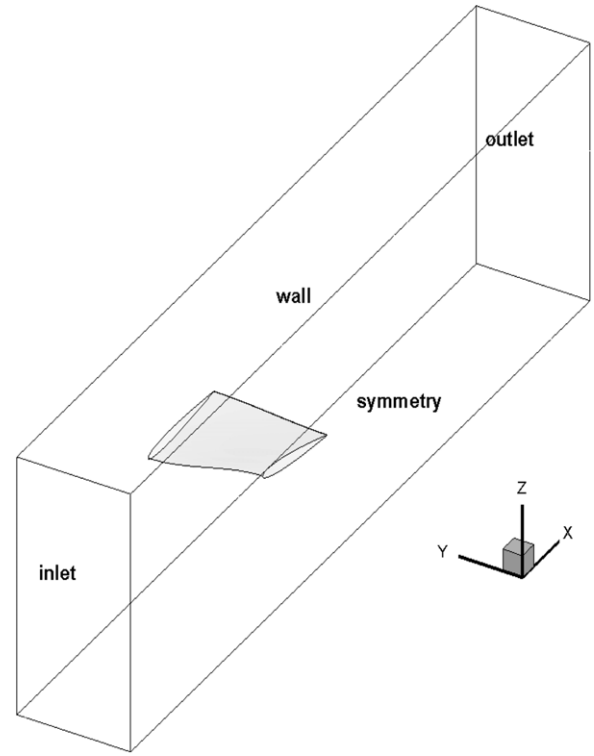

Fig. 2. Computational domain and boundary condition.

where p_{out} is the static pressure of outlet, 29.0 kPa. p_v is the vapor pressure, 2.97 kPa. ρ_l is the water density, 998.0 kg/m^3. V_∞ is the inflow velocity, 6.97 m/s, thus the cavitation number is $\sigma = 1.07$.

The Reynolds number is defined as

$$\mathrm{Re} = \frac{\rho_l V_\infty C}{\mu}. \tag{16}$$

where C is the chord length of the hydrofoil 0.15 m, which is treated as the characteristic length. μ is the water dynamic viscosity, 0.001003 kg/ms. Thus the Reynolds number is $\mathrm{Re} = 1.04\times10^6$.

The computational domain is shown in Fig. 2. Only half of the hydrofoil and the surrounding channel space is used in the numerical simulations on account of the geometric symmetry. The hydrofoil was located in a channel with a height $2\times C$, a length of $2\times C$ upstream of the leading edge, a length of $5\times C$ downstream of the leading edge and a width of C. The boundary conditions consisted of an imposed velocity at the inlet, a fixed static pressure at the outlet with free slip wall conditions at the upper and lower walls and non-slip walls on the hydrofoil and a symmetry boundary on the midplane. A C–H type grid is generated for the domain with sufficient refinement near the foil surface as shown in Fig. 3. It is noted that the value of y^+ calculated at the first grid point away from the hydrofoil surface in the wall normal direction is around 1. The grid growth rate is 1.05.

Two sets of grid are used to study the influence of mesh resolution on the results (Figs. 4 and 5). The information of grid settings is listed in Table 1. The grid spacing in Fig. 4 (the coarse mesh)in the stream-wise, wall-normal and span-wise directions are 1 mm (approximately 100 wall units), 0.01 mm (approximately 1 wall units) and 3.75 mm (approximately 375 wall units). The grid spacing(the fine mesh) in Fig. 5 in the stream-wise, wall-normal and span-wise directions are 0.69 mm (approximately 69 wall units), 0.01 mm (approximately 1 wall units) and 1.5 mm (approximately 150 wall units). Compared to the coarse mesh, the cells are refined both in the spanwise direction (A) and the chord direction (B + C + D) of hydrofoil in the fine mesh.

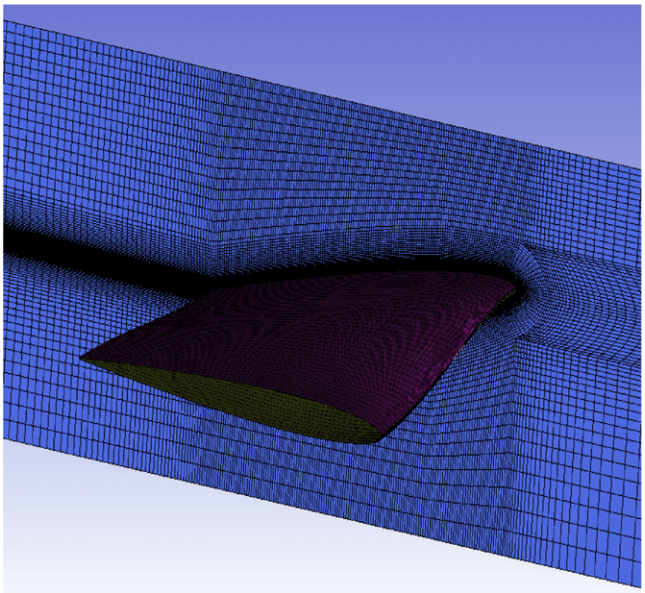

Fig. 3. Mesh generation around the twisted hydrofoil surface ($\alpha = -2°$).

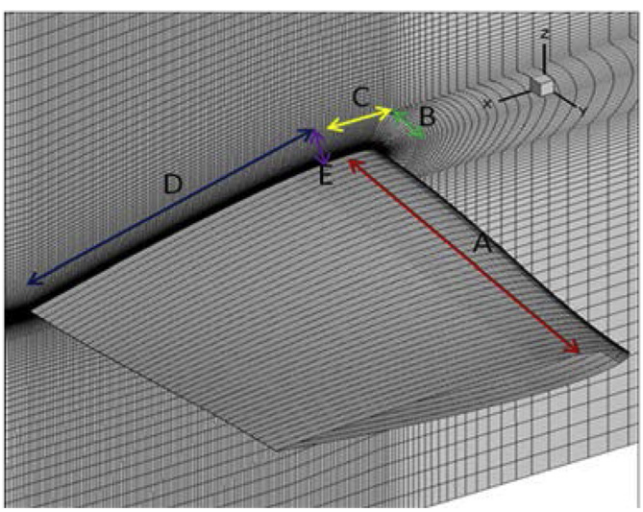

Fig. 4. Grid settings (coarse)-2 million.

Table 1
Grid settings: nodes numbers.

	Coarse mesh (2 million)	Fine mesh (10 million)
A	40	100
B	15	25
C	35	70
D	100	121
E	65	120

Traditionally, near walls in boundary layers the size of turbulent eddies scales roughly as the distance from the wall, limited by viscous scales, which means that well resolved LES requires grids nearly as fine as those used in direct numerical simulation (DNS). This restriction applies not only to wall-normal grid spacing but to horizontal grid spacing as well. But the cost is not affordable in the simulation of high Reynolds number turbulent flow, which is still restricted by computer power. Thus LES with wall stress models [33] is adopted here. The objective with wall stress models is to supply to the simulation of the outer flow the viscous stresses or drag due to the sharp velocity gradient at the walls, which cannot otherwise be calculated on the very coarse LES grid. Wall

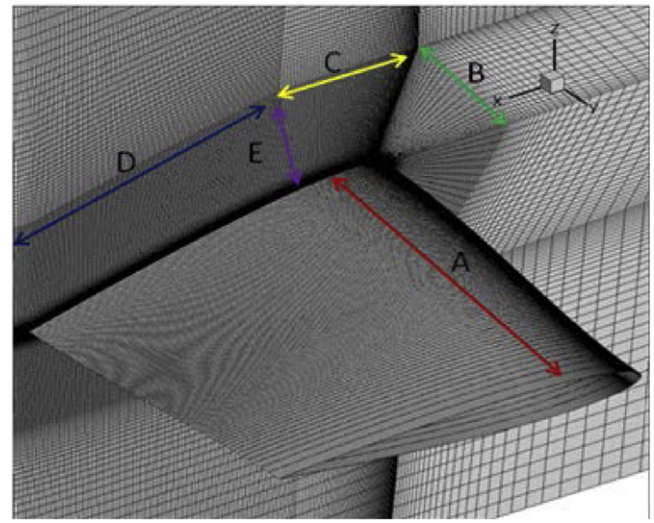

Fig. 5. Grid settings (fine)-10 million.

stress models generally use information from outer flow near the wall to set the level of wall stress, which allows them to respond to varying conditions in the outer flow. Thus, the grid spacing in the wall-normal direction set to be 1 wall units. The grid spacing on the stream-wise and span-wise directions can be set according to that in the outer flow domain. Compared with the DNS method, LES can get rid of the limitations in simple modeling and affordable cost, which is most suitable for unsteady three-dimensional complex turbulent flows in industry and natural environment [34].

The simulation of non-cavitating flow is carried out with the coarse mesh. The detailed results are shown in the Appendix. The lift forces and pressure distributions obtained in numerical simulations agree well with the experimental results for the fully wetted flow conditions (as shown in Figs. 21 and 22).

Simulations on cavitating flow are conducted by using the open source code OpenFOAM. The first-order implicit scheme is employed for time discretization and Gauss linear interpolation for spatial discretization. A various time step is used by setting the global maximum Courant number as 0.2. The average time step is less than 1 μs through the simulation.

3. Results and discussion

3.1. Cavity shapes in a shedding cycle

The length of the cavity, L_{cav}, represents the transient behavior of cavitating flows. The definition of the cavity length is shown in Fig. 6, the images are taken from Ref. [10]. As shown in the sketch, the red line marks cavitation shedding interface, cavity length is the distance from the hydrofoil leading edge to the red line in the symmetry plane.

The comparison of cavity lengths between the experimentally measured results and the LES results with the fine mesh is shown in Fig. 7. The lengths of cavities are gotten through measuring the pixels in pictures. For example, the hydrofoil in which the chord length is 150 mm is about 488 pixels in pictures in numerical results. Then, 1 pixel stands for 0.31 mm, and the deviation is 0.31 mm. The chord length is about 730 pixels in experimental results. 1 pixel stands for 0.21 mm, and the deviation is 0.21 mm. The development of cavity length is periodic. The shedding cycle and cavity lengths calculated by LES with the fine mesh are in good agreement with experimental results. The experimentally measured shedding frequency is $f = 32.2$ Hz [10] and the calculated shedding frequency by LES is $f = 30.12$ Hz. The deviation is 6.5%.

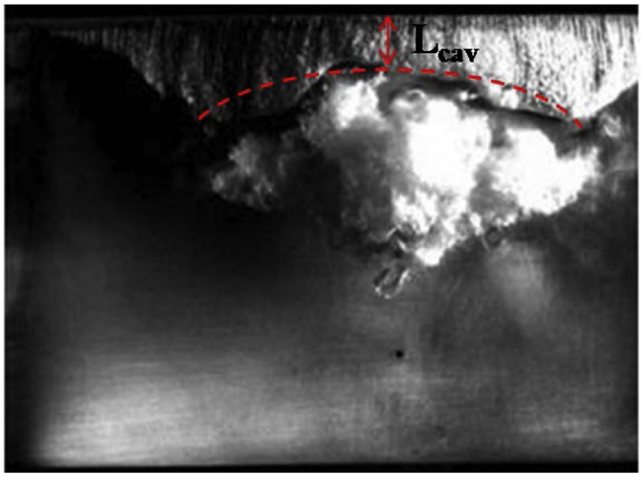

Fig. 6. The definition of the cavity length [10]. (For interpretation of the references to color in this figure legend, the reader is referred to the web version of this article.)

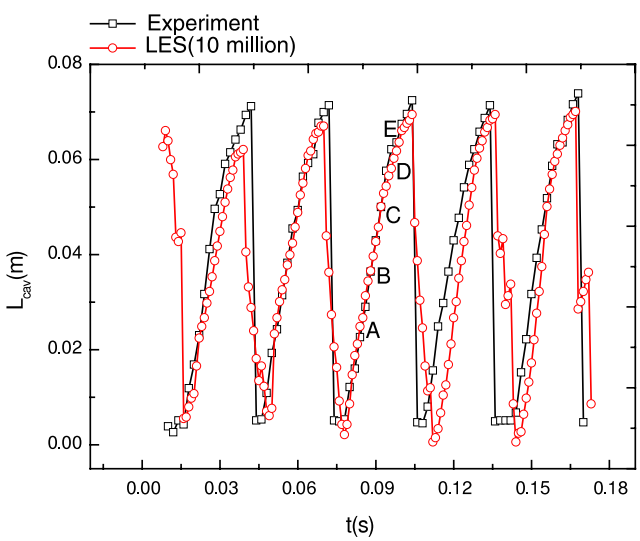

Fig. 7. Cavity length—experiment and LES (10 million).

Fig. 8 represents the comparison of cavity lengths change with two sets of grids. The maximum cavity length calculated by the coarse mesh is 0.073 m, and is 0.069 m got by the fine mesh. The cavity shedding frequency is 22.99 Hz for the coarse mesh which is remarkably different with the fine mesh. With the increase of grid quantity, the cavitation shedding period is shortened by 24%. The cavity length is shortened by 5.8% which is smaller than the error of frequency. The reason may be caused by the velocity of re-entry jet V. The cavitation shedding frequency (f) has a dimension of $\frac{V}{L}$. V mainly represents the velocity of re-entry jet, and L is the cavity length. Therefore, except for the length, the velocity of re-entry jet is another important influencing factor of frequency. The velocity of re-entry jet can be gotten in Fig. 17. The negative velocity is identified as the velocity of re-entry jet. It is indicated that the mesh resolution has a greater impact on the velocity of re-entry jet. For example, with the increase of grid quantity, the maximum value of re-entry velocity is shortened by 24% at the instant C. Consequently, the cavity length error is smaller than the error of frequency.

Next, Cavity shape and cavitation patterns are obtained to discuss the influence of mesh to the cavity evolution. In order to describe the cavity development process in detail, five typical instants of cavitating flows are selected (as shown in Fig. 7(A)–(E)). The time interval between the adjacent instants is 0.004 s. The

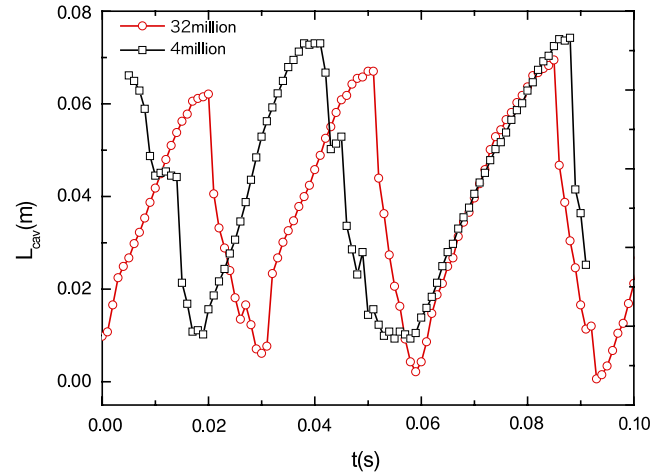

Fig. 8. Cavity length—10 million and 2 million.

hydrofoil cross-section is different, so the flow pattern shows notable three-dimensional features. The re-entrant jet is not symmetrical, but its frontier forms as an arc-shaped curve. The cavity shape got by the experiment at every instant is shown in Fig. 9 [10]. The main horseshoe vortex shedding (as shown in Fig. 9(B) with the arrows pointed to) and secondary horse-shoe vortex shedding (as shown in Fig. 9(B) with the arrows pointed to) are formed, which is very different from two-dimensional cavitating flows.

Cavitation patterns during one cavity shedding cycle in the fine mesh results are shown in Fig. 10. At instant A, the cavity length is generated from the leading edge, and then the shedding cloud becomes more turbulent and is advected downstream by the main flow. At instant B, it is noted that the primary shedding cloud becomes two horse-shoe vortices structure. These two vortices intertwine each other and then flow downstream. At instant C, a pair of small cavities appeared in the positions of both sides of the main cavity. Finally at the instant D and E, the main shedding cavity collapses at the closure. The cavity in the symmetric plane is longer than cavities in other planes which are parallel to the flow direction, and the shedding cavity is also the largest in the middle. That is because the actual attack angle of hydrofoil section decreases from the middle to the end in the spanwise direction. The calculation results obtained from the cavitation patterns and the cavity shedding position are in good agreement with the experimental observations in Fig. 9 [10].

Fig. 11 represents the cavitation patterns during one shedding cycle with the coarse mesh. Compared with the Fig. 10, two horse-shoe vortices structure in instant B and a pair of small cavity at instant C are not captured clearly.

The comparison between the results of Ji's and ours has also been discussed here. Partially-Averaged Navier–Stokes (PANS) model is used with a mixture model to simulate the unsteady cavitating flow around the Delft twisted hydrofoil by Ji [22]. The PANS model is a bridging method from the RANS to DNS. The commercial CFD code ANSYS-CFX is used to implement PANS model. The turbulent governing equations in the PANS model are from the standard k–ε model. The Zwart model derived from a simplified Rayleigh–Plesset equation which neglects the second order derivative of the bubble radius is used for the cavitation simulation. The medium resolution mesh with about 3 million nodes was selected as the final grid. The predicted shedding frequency was about 30.7 Hz in Ji's article [22].

The open source code OpenFOAM is used to simulate the cavitating flow in this paper. The k–μ model is introduced to calculate the transport equation of SGS. VOF model and Kunz cavitation model are adopted to consider the interaction between

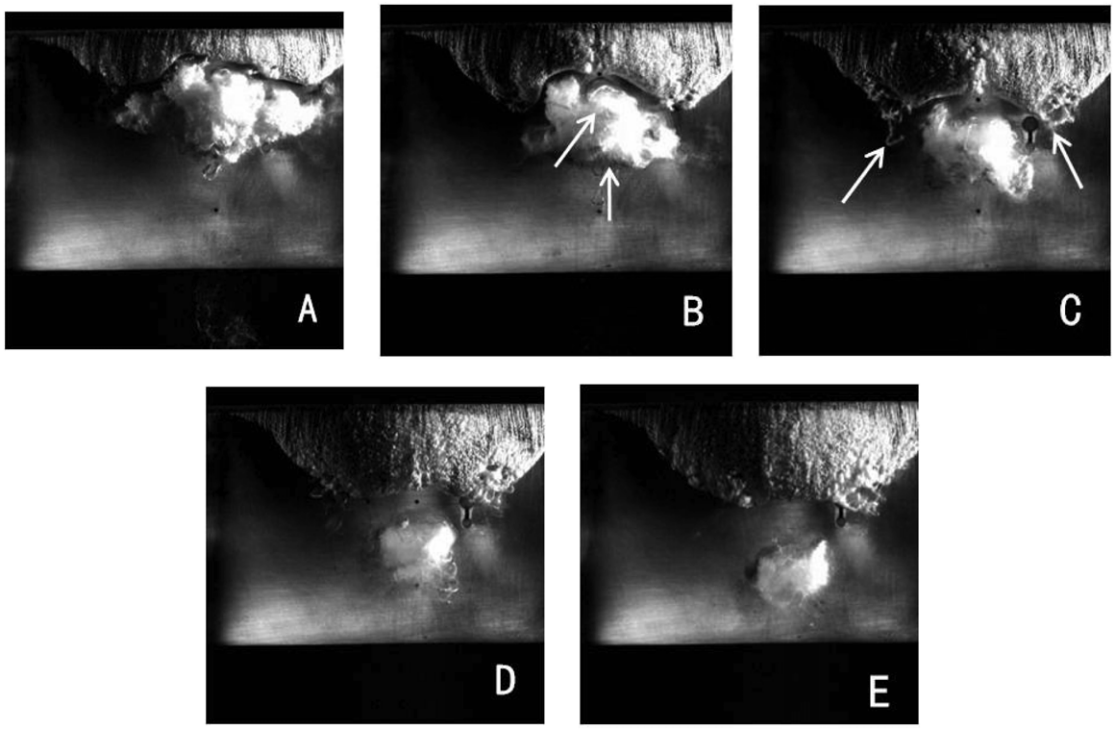

Fig. 9. Cavitation patterns during one cavity shedding cycle—experiment result [10].

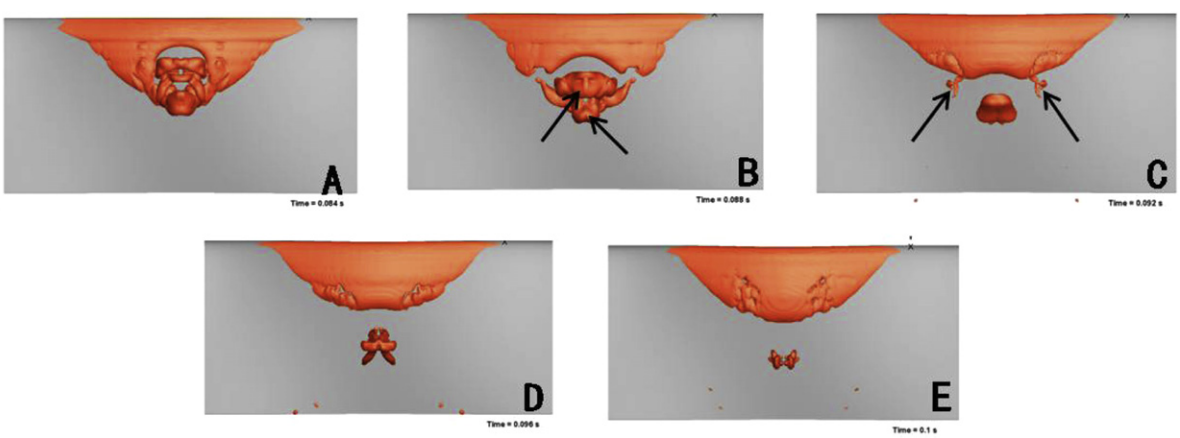

Fig. 10. Cavitation patterns during one shedding cycle (simulation with the fine mesh).

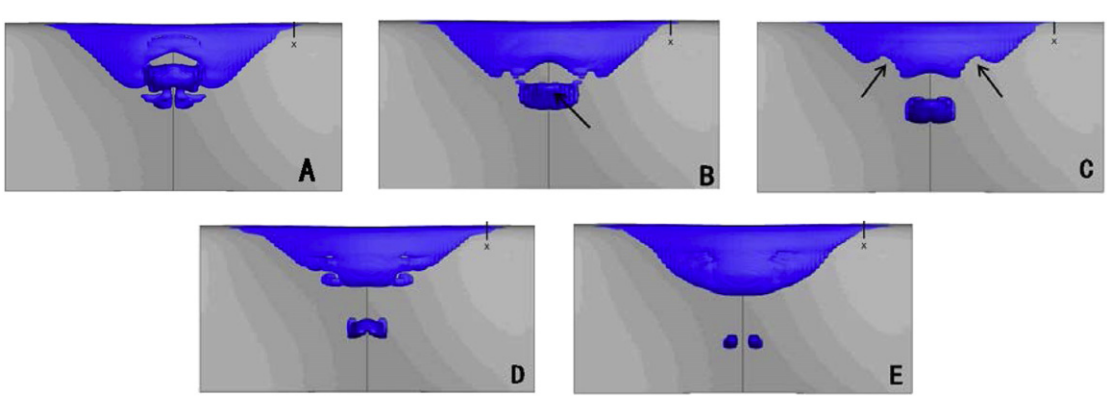

Fig. 11. Cavitation patterns during one cavity shedding cycle (simulation with the coarse mesh).

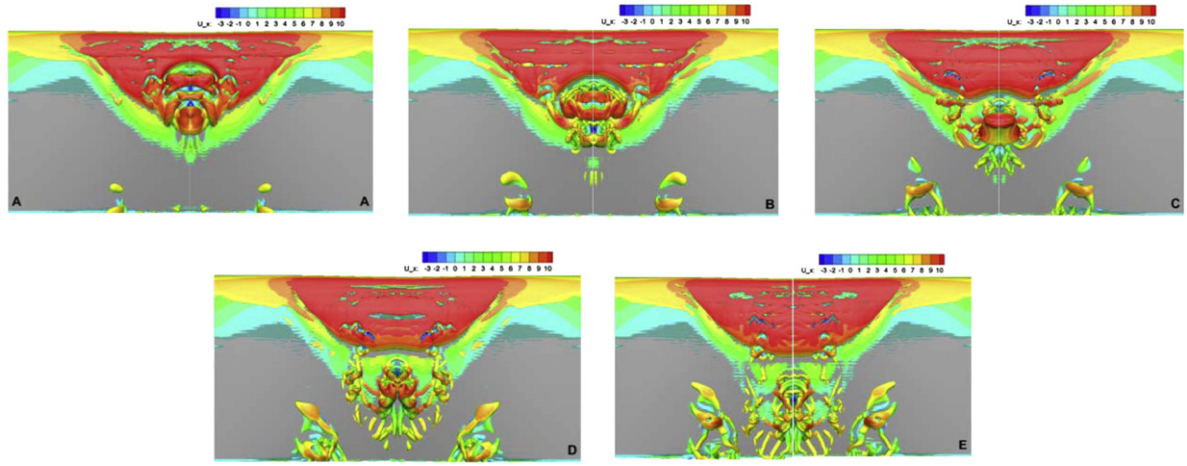

Fig. 12. Isosurface of Q distribution(simulation with the fine mesh, the color represents the flow velocity in the chord direction). (For interpretation of the references to color in this figure legend, the reader is referred to the web version of this article.)

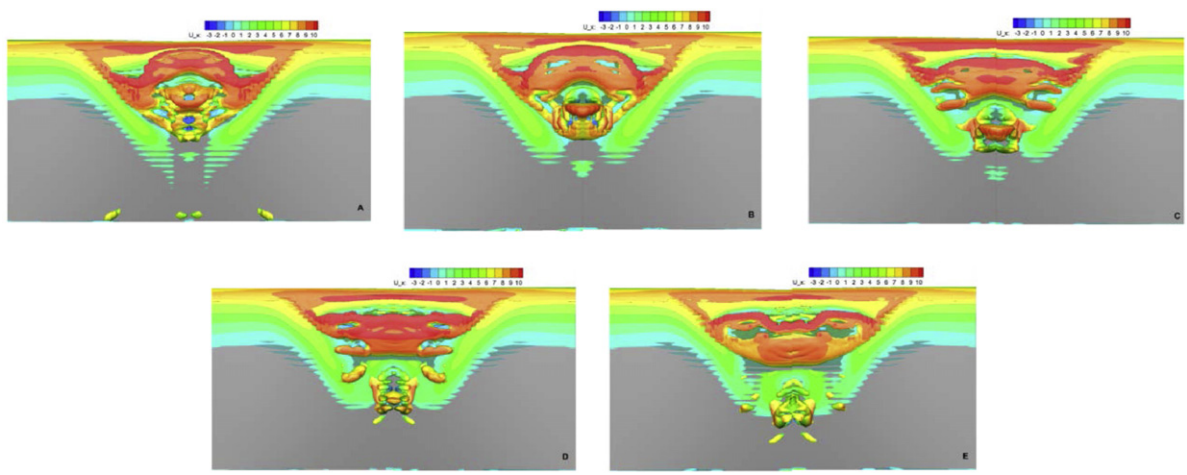

Fig. 13. Isosurface of Q distribution(simulation with the coarse mesh, the color represents the flow velocity in the chord direction). (For interpretation of the references to color in this figure legend, the reader is referred to the web version of this article.)

water and vapor phases. Two set of grids—10 millon and 2 million nodes are calculated. The shedding frequency with 10 million nodes is 30.12 Hz and 22.99 Hz with 2 million nodes.

The experimentally measured shedding frequency is $f = 32.2$ Hz [10]. The shedding frequency got by the PANS method with 3 million nodes [22] and LES method with 10 million nodes agrees fairly well with the measured frequency. The frequency deviation between the two methods is 1.9%. Cavitation patterns are compared with the two methods (as shown in Ji's article—Fig. 8 in Ref. [22] and Fig. 10 in this paper). Compared to PANS method, the LES method can describe the cavity shape more clearly in detail. But the PANS method has less demanding on the grid resolution.

3.2. Vortex shedding evolutions

In order to illustrate the evolution of shedding horse-shoe vortex structure effectively, the flow structures are visualized based on the Q-criterion, defined as the second invariant of the velocity gradient tensor, are given by

$$Q = 1/2\left(|\Omega|^2 - |S|^2\right) \tag{17}$$

where Ω is the vorticity tensor, S is the strain tensor. The criterion for vortex generated was $Q > 0$, which means that the rotating parts play a dominant role in the velocity gradient tensor region.

For the present case, the iso-surface of the Q-criterion is set as 200 000 to visualize the vortex structures in the turbulent cavitating flow. It can be seen that more refined shedding vortices are captured with the fine mesh (as shown in Figs. 12 and 13). The main vortices are similar in the flow direction with the two sets of meshes, representing as double vortex twining each other, while the vortex with the fine mesh is wider in the spanwise direction (as shown in the Figs. 12(B) and 13(B)). The secondary vortex in the fine mesh results is horse-shoe shaped and shedding at the corner of the main cavity profile (as shown in Fig. 12(C)/(D)/(E)), which is very similar with the experimental results. Nevertheless, there is no obvious secondary vortex shedding in the coarse mesh results. The vortices shed like wave structures at the corner (as shown in Fig. 12(C)/(D)).

The local vortex structure is displayed in Fig. 14 to discuss the effect of mesh. The small size shedding vortex can only be captured by the fine mesh, and the mesh density in the spanwise direction is important to describe the shedding of small scale vortex.

3.3. The 3D structures of re-entry jets

Re-entry jet is the key factor on the shedding of cavity and vortex, which has been widely studied. Re-entry jet is a transparent liquid stream, which is opposite to the direction of the main flow in the cavity. Re-entry jet is produced by the adverse pressure gradient near the closure the cavities. The re-entry jets in two-dimensional and three dimensional cavities have been observed by high-speed video [3,35]. The structure of the two-phase flow inside

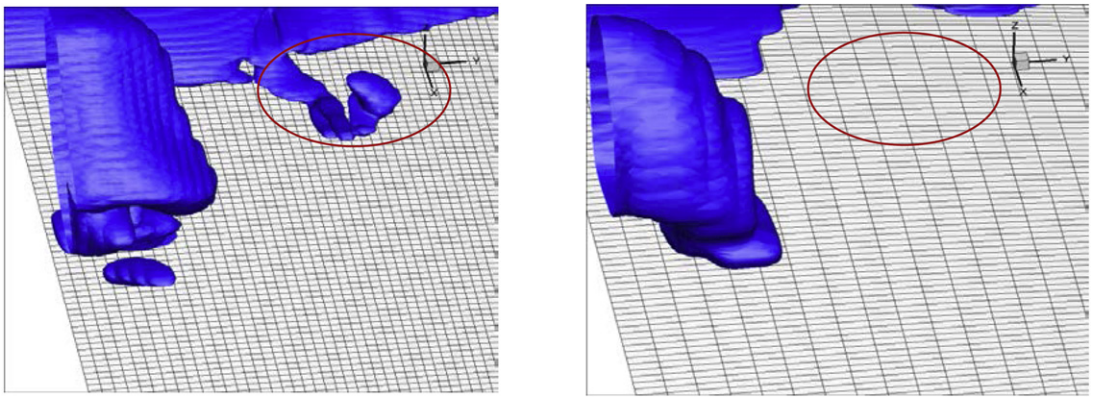

Fig. 14. Local vortex structure (left-fine mesh, right-coarse mesh).

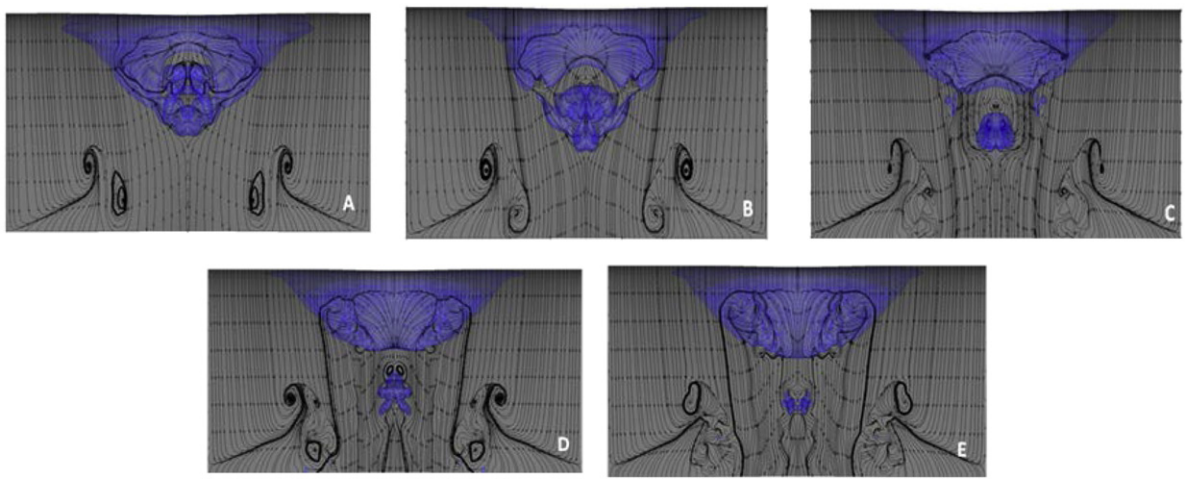

Fig. 15. The surface streamlines together with the isosurface of vapor fraction $\alpha_v = 0.9$ (simulation with the fine mesh).

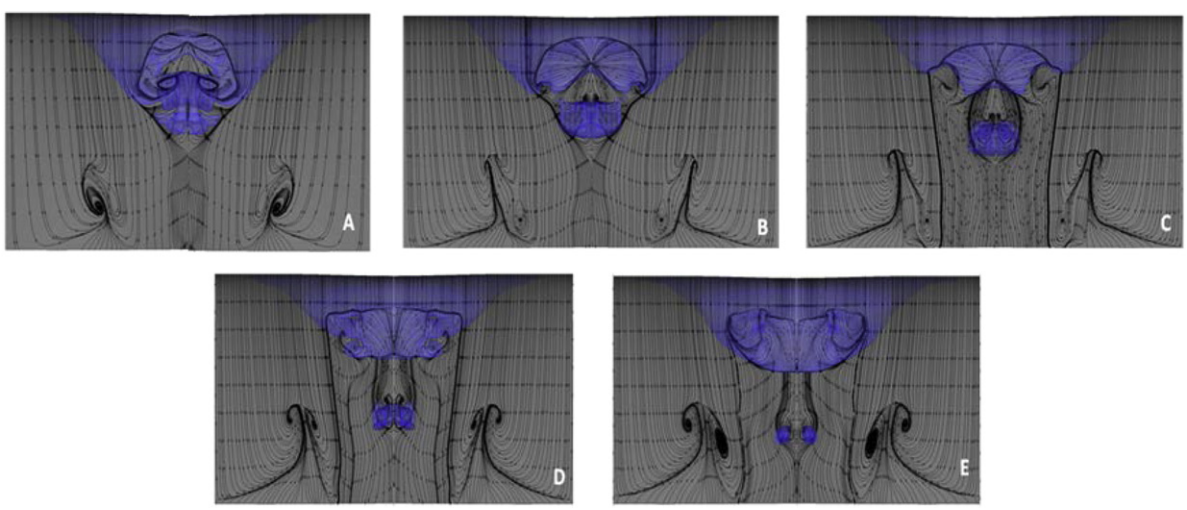

Fig. 16. Cavity image isosurface of vapor fraction at $\alpha_v = 0.9$ together with the velocity streamlines (simulation with the coarse mesh).

the cavity has also been investigated by using a double optical probe [36]. It indicates that the formation of a re-entrant jet is the main reason for the unsteadiness. The cavity will be cut off by the re-entry jet. Then the shedding cavity collapses which leads to a high pressure in local domain. Another re-entry jet will be induced accordingly. Thus the re-entry jet plays a significant function in the vapor cloud shedding process.

For the flow around the twisted hydrofoil, the frontier of the re-entry jet is curved. The surface streamlines together with the isosurface of vapor fraction $\alpha_v = 0.9$ are shown in Fig. 15 (with the fine mesh) and Fig. 16 (with the coarse mesh). The re-entry jet is generated from the cavity closure in the symmetry plane and flows around as a three dimensional condition. The frontier profile where the re-entry jet intersects with the main flow is semi-elliptic. The spanwise width in the fine mesh results is larger than that with the coarse mesh. Because the re-entry jet is induced by the pressure gradient, it is possible that the spanwise pressure gradients are different with the two meshes.

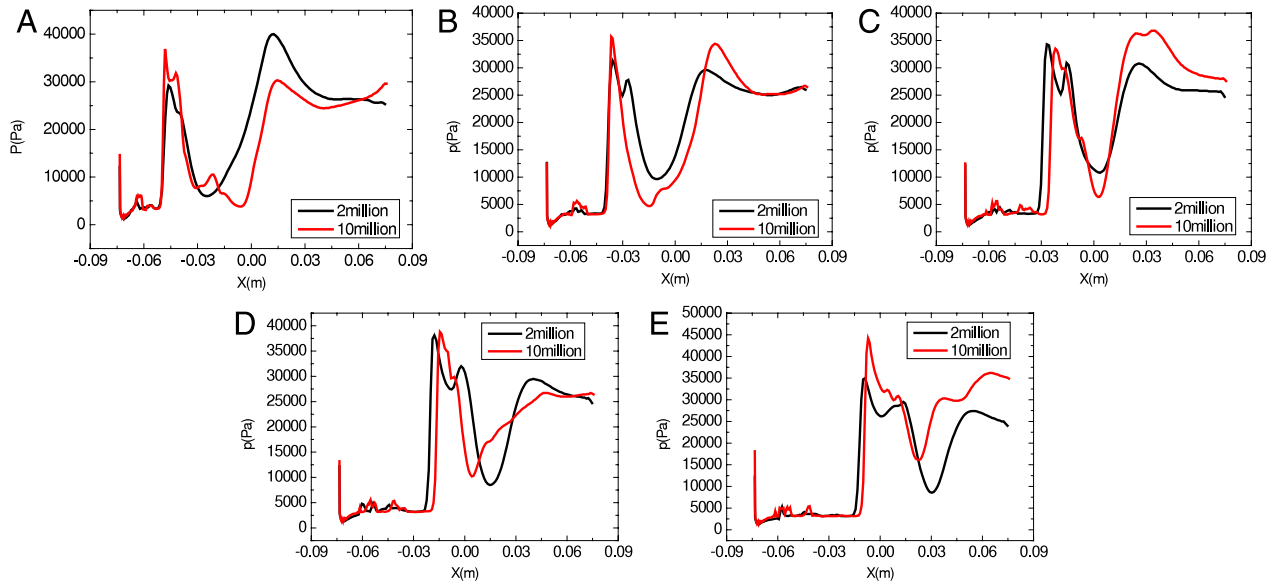

Fig. 17. Pressure distribution in the flow direction.

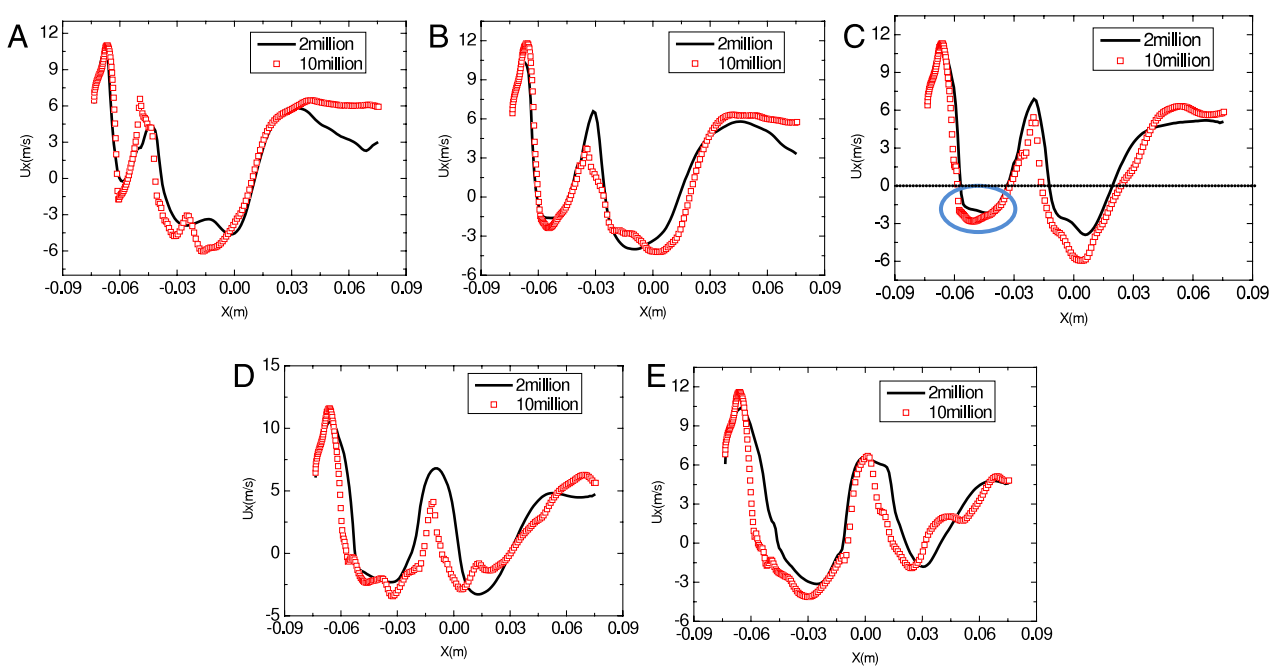

Fig. 18. Velocity components distribution in the flow direction.

3.4. Pressure and velocity distributions in the flow direction

To further analyze the mesh effect, the pressure distribution and velocity components distribution along the lines in the flow direction are obtained (as shown in Figs. 17 and 18). The line in Fig. 17 is derived from the middle line of the 3-D twisted wing, and the pressure data are obtained along this line. The line in Fig. 18 is defined by enlarging the line in Fig. 17 by 1% in the stream-wise and wall-normal directions. The zoom origin is fixed at the axis center of the middle line. The near wall velocity data are obtained along the enlarged line. The nodes numbers (B + C + D in Figs. 4 and 5) in the flow direction on the hydrofoil are 150 in the coarse mesh and 216 in the fine mesh, respectively. The difference of U_x and P between the two sets of meshes is small, such as the length, the velocity of the re-entry jet and the pressure peak values at the cavity closure. Thus the grid quantity in this direction is enough and has little effect on the results.

3.5. Pressure distributions in the spanwise direction

Fig. 19 represents the pressure distributions in the spanwise direction at instant A with different X. X is the distance from the leading edge of hydrofoil. At this moment, the cavity starts to shed in the symmetric plane. The cavity closure is at $X = 3.5$ cm where the pressure distributions are similar with different meshes. However there is a pressure peak at $X = 5.5$ cm in the middle of the bubble with the fine mesh (as shown in Fig. 20). That is because the cavity breaks up in the spanwise direction there which can be only obtained with the fine mesh (as the arrow pointed to in Fig. 20).

The pressure distributions in the spanwise direction at instant B–E are similar with what are shown in Figs. 19 and 20. The resolution in spanwise direction of coarse mesh is not insufficient to capture the cavity shedding and collapse pressure, which will

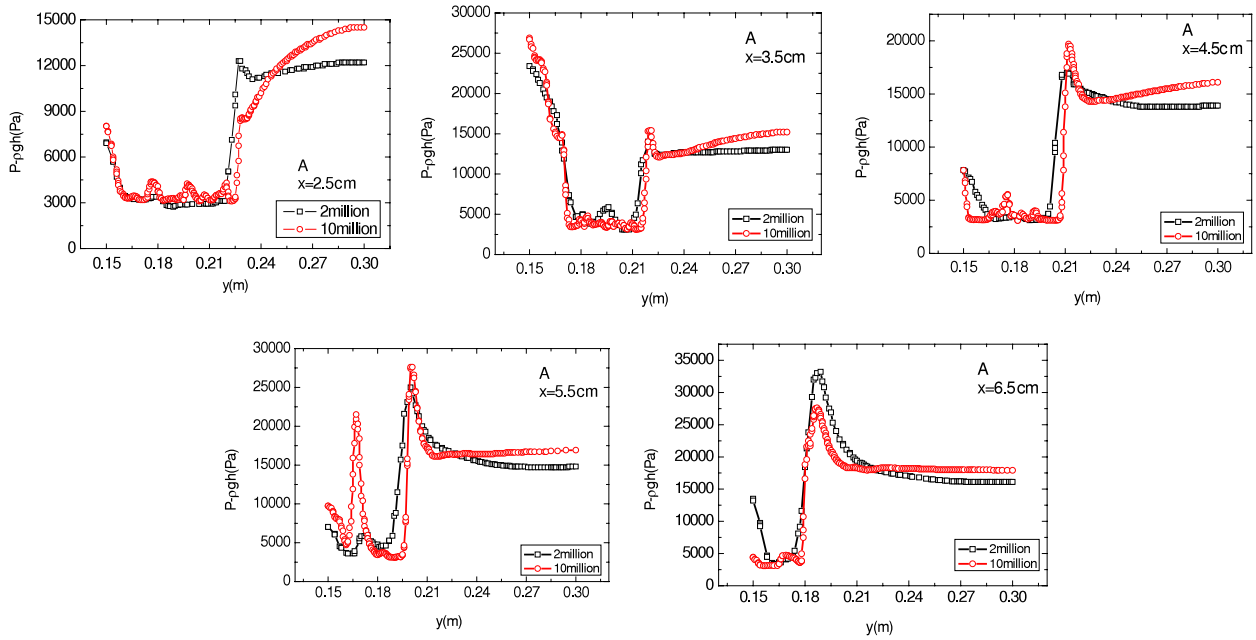

Fig. 19. Pressure distribution in the spanwise direction (A).

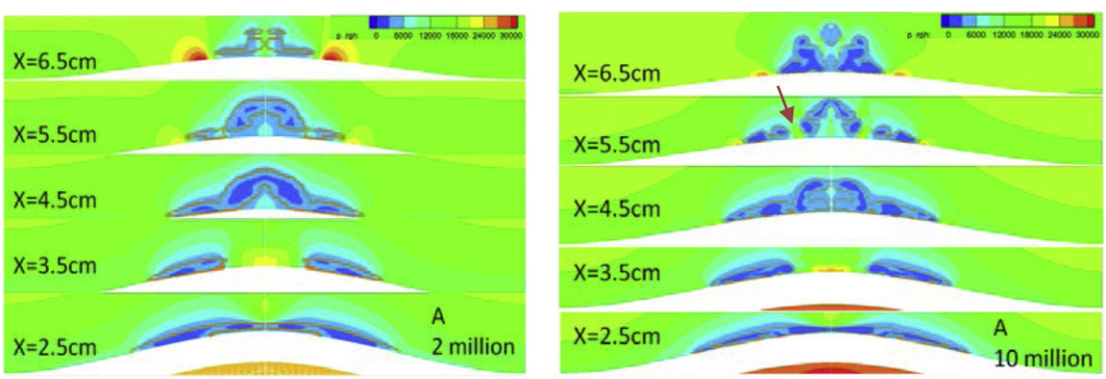

Fig. 20. Pressure distribution and cavity pattern in the slices at different X positions (at instant A, the color represents the pressure distribution and the line shows the bubble boundary). (For interpretation of the references to color in this figure legend, the reader is referred to the web version of this article.)

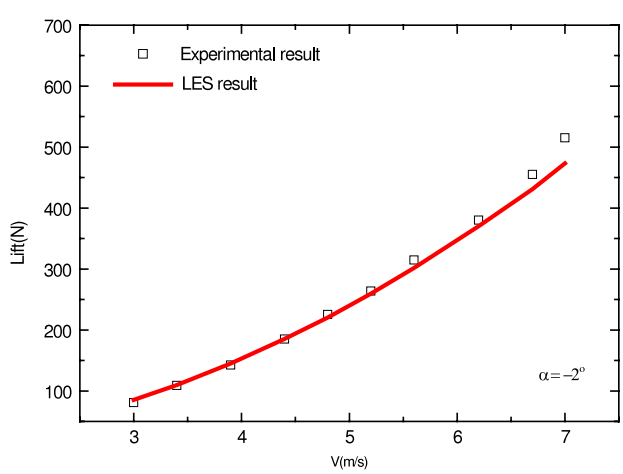

Fig. 21. The lift curve with flow velocity at -2° angle of attack.

result in velocity reduction of re-entry jet. Thus the cavity develops more easily in the flow direction, and the cavity in the coarse mesh results is longer and the shedding frequency is lower than those with fine mesh and in experiments results.

4. Conclusions

Unsteady cavitating turbulent flow around a three dimensional twisted wing is simulated by using large eddy simulation method. Based on the numerical results and the comparisons between two sets of meshes, several conclusions can be drawn as follows:

(1) The grids resolution has remarkable influence on the cavity length, cavity shedding periodic and cavitation patterns. Results with fine mesh (10 million) in the present paper agree well with the experimental results.
(2) Although the coarse grid has enough precision in the calculation of fully wetted flow, the small scale shedding vortex cannot be captured in the simulation of the cavitating flow.
(3) More spanwise nodes are needed for cavitating flow simulation. The re-entry jet in spanwise direction can affect the overall development of cavities, which is sensitive to the pressure gradient and spanwise resolution of the mesh.

Acknowledgments

The authors are grateful to the Science and technology innovation project of Chinese Academy of Sciences through grant

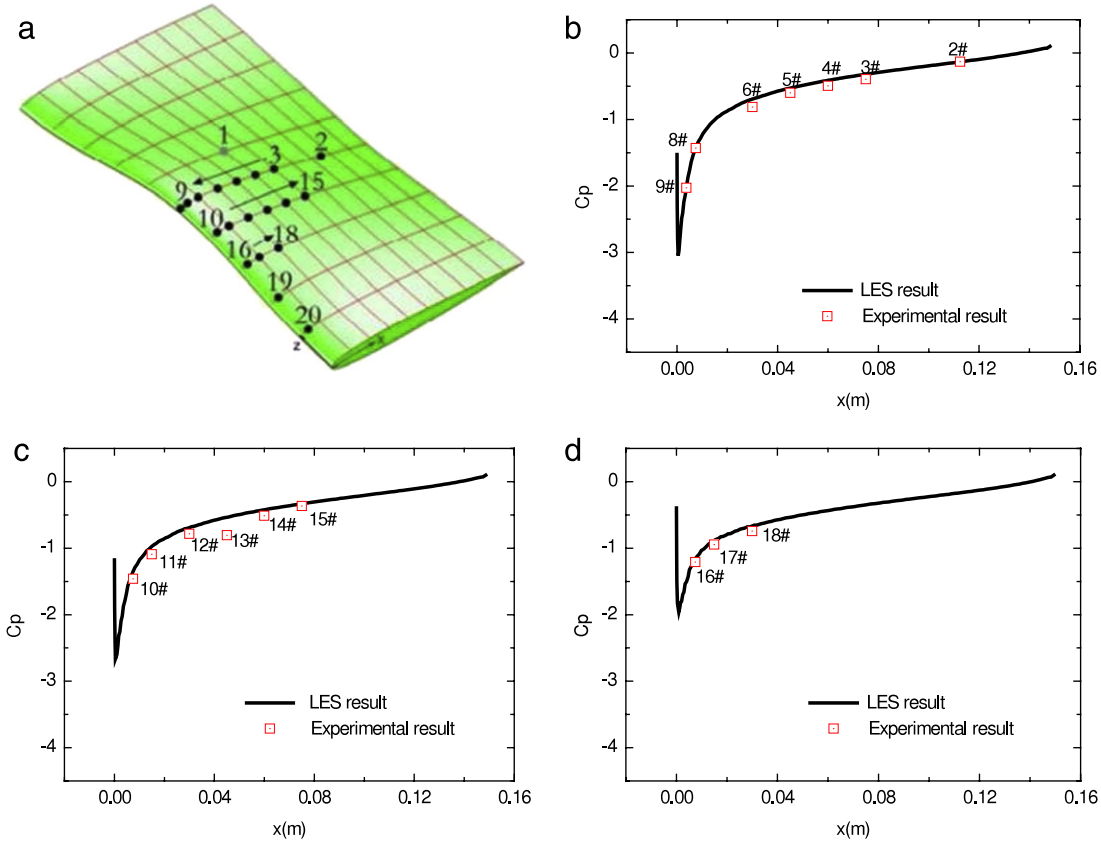

Fig. 22. The pressure coefficient distribution with flow velocity at −2° angle of attack.

numbers KGFZD-125-014, National Natural Science Foundation of China through grant numbers 11202215&11332011 and the Youth Innovation Promotion Association of CAS (2015015).

Appendix. Computation of fully wetted flow

The coarse mesh with 2 million cells is used to compute the hydrodynamic force in fully wetted flow. Mesh generation method is similar to that in Fig. 3, and the value of y^+ calculated at the first grid point away from the hydrofoil surface in the wall normal direction is also kept around 1.

The lift curve with flow velocity at −2° angle of attack is shown in Fig. 21. The average error between the experiment result and numerical result is smaller than 5%.

A series of pressure sensors are set on the surface of the hydrofoil to obtain the pressure distribution. The layout and serial number of the pressure sensors are shown in Fig. 22(a) [10]. The comparison of pressure coefficient between experimental result and numerical result are given in Fig. 22(b)–(d). It is noted that the calculation result has been able to capture the hydrofoil surface pressure distribution accurately for the coarse mesh, which means that this mesh quantity is good enough for the simulations of fully wetted flow.

References

[1] K.R. Laberteaux, S.L. Ceccio, Partial cavity flows. Part 2. Cavities forming on test objects with spanwise variation, J. Fluid Mech. 431 (2001) 43–63.
[2] M. Dular, R. Bachert, C. Schaad, B. Stoffel, Investigation of a re-entrant jet reflection at an inclined cavity closure line, Eur. J. Mech. B Fluids 26 (2007) 688–705.
[3] D.F. de Lange, G.J. de Bruin, Sheet cavitation and cloud cavitation, re-entrant jet and three-dimensionality, Appl. Sci. Res. 58 (1997) 91–114.
[4] J. Dang, G. Kuiper, Re-entrant jet modeling of partial cavity flow on two-dimensional hydrofoils, J. Fluids Eng. 121 (1999) 773–780.
[5] Y. Saito, R. Takami, I. Nakamori, T. Ikohagi, Numerical analysis of unsteady behavior of cloud cavitation around a NACA0015 foil, Comput. Mech. 40 (2007) 85–96.
[6] G.H. Schnerr, I.H. Sezal1, S.J. Schmidt, Numerical investigation of three-dimensional cloud cavitation with special emphasis on collapse induced shock dynamics, Phys. Fluids 20 (2008) 040703.
[7] S. Park, S.H. Rhee, Numerical analysis of the three-dimensional cloud cavitating flow around a twisted hydrofoil, Fluid Dynam. Res. 45 (2013) 201–218.
[8] E.J. Foeth, C.W.H.V. Doorne, T.V. Terwisga, B. Wieneke, Time resolved PIV and flow visualization of 3D sheet cavitation, Exp. Fluids 40 (2006) 503–513.
[9] E.J. Foeth, T.V. Terwisga, C.V. Doorne, On the collapse structure of an attached cavity on a three-dimensional hydrofoil, J. Fluids Eng. 130 (2008) 071303.
[10] E.J. Foeth, The structure of three-dimensional sheet cavitation (Doctoral Thesis), Delft University of Technology, Wageningen, The Netherlands, 2008.
[11] L.X. Zhang, B.C. Khoo, Computations of partial and super cavitating flows using implicit pressure-based algorithm (IPA), Comput. & Fluids 73 (2013) 1–9.
[12] D.C. Wilcox, Turbulence Modeling for CFD, second ed., DCW Industries, Inc., 1998.
[13] Y. Chen, C.J. Lu, A homogenous-equilibrium-model based numerical code for cavitation flows and evaluation by computation cases, J. Hydrodyn. 20 (2008) 186–194.
[14] D.O. Coutier, J.L. Reboud, Y. Delannoy, Numerical simulation of the unsteady behaviour of cavitating flows, Internat. J. Numer. Methods Fluids 42 (2003) 527–548.
[15] J. Decaix, E. Goncalves, Compressible effects modeling in turbulent cavitating flows, Eur. J. Mech. B Fluids 39 (2013) 11–31.
[16] E. Goncalves, Numerical study of unsteady turbulent cavitating flows, Eur. J. Mech. B Fluids 30 (2011) 26–40.
[17] B. Huang, Y.L. Young, G.Y. Wang, W. Shyy, Combined experimental and computational investigation of unsteady structure of sheet/cloud cavitation, J. Fluids Eng. 135 (2013) 071301.
[18] Y.W. Wang, L.J. Liao, T.Z. Du, C.G. Huang, Y.B. Liu, X. Fang, N.G. Liang, A study on the collapse of cavitation bubbles surrounding the underwater-launched projectile and its fluid–structure coupling effects, Ocean Eng. 84 (2014) 228–236.
[19] D.M. Liu, S.H. Liu, Y.L. Wu, H.Y. Xu, LES numerical simulation of cavitation bubble shedding on ale 25 and ale 15 hydrofoils, J. Hydrodyn. Ser. B 21 (2009) 807–813.
[20] R.E. Bensow, G. Bark, Implicit LES predictions of the cavitating flow on a propeller, J. Fluids Eng. 132 (2010) 041302.
[21] N.X. Lu, R.E. Bensow, G. Bark, Large eddy simulation of cavitation development on highly skewed propellers, J. Mar. Sci. Technol. 19 (2014) 197–214.

[22] B. Ji, X.W. Luo, Y.L. Wu, X.X. Peng, Y.L. Duan, Numerical analysis of unsteady cavitating turbulent flow and shedding horse-shoe vortex structure around a twisted hydrofoil, Int. J. Multiphase Flow 51 (2013) 33–43.
[23] B. Ji, X.W. Luo, X.X. Peng, Y.L. Wu, Three-dimensional large eddy simulation and vorticity analysis of unsteady cavitating flow around a twisted hydrofoil, J. Hydrodyn. 25 (2013) 510–519.
[24] B. Ji, X.W. Luo, R.E.A. Arndt, Y.L. Wu, Numerical simulation of three dimensional cavitation shedding dynamics with special emphasis on cavitation–vortex interaction, Ocean Eng. 87 (2014) 64–77.
[25] B. Huang, Y. Zhao, G.Y. Wang, Large eddy simulation of turbulent vortex-cavitation interactions in transient sheet/cloud cavitating flows, Comput. & Fluids 92 (2014) 113–124.
[26] G.M. Wang, O. Starzewski, Large eddy simulation of a sheet/cloud cavitation on a Naca0015 hydrofoil, Appl. Math. Model. 31 (2007) 417–447.
[27] B. Ji, X.W. Luo, R.E.A. Arndt, X.X. Peng, Y.L. Wu, Large Eddy Simulation and theoretical investigations of the transient cavitating vortical flow structure around a NACA66 hydrofoil, Int. J. Multiphase Flow 68 (2015) 121–134.
[28] E. Roohi, A.P. Zahiri, P.F. Mahmud, Numerical simulation of cavitation around a two-dimensional hydrofoil using VOF method and LES turbulence model, Appl. Math. Model. 37 (2013) 6469–6488.
[29] P. Sagaut, Large Eddy Simulation for Incompressible Flows, third ed., Springer, Berlin, 2006.
[30] F. Nicoud, F. Ducros, Subgrid-scale stress modelling based on the square of the velocity gradient tensor, Flow Turbul. Combust. 62 (1999) 183–200.
[31] F.M. Passandideh, E. Roohi, Transient simulations of cavitating flows using a modified Volume-of-Fluid (VOF) technique, Int. J. Comput. Fluid Dyn. 22 (2008) 97–114.
[32] R.F. Kunz, D.A. Boger, D.R. Stinebring, T.S. Chyczewski, J.W. Lindau, H.J. Gibeling, S. Venkateswaran, T.R. Govindan, A preconditioned Navier–Stokes method for two-phase flows with application to cavitation prediction, Comput. Fluids 29 (2000) 849–875.
[33] J.C. Li, Large eddy simulation of complex turbulent flows: physical aspects and research trends, Acta Mech. Sin. 17 (2001) 289–301.
[34] W. Cabot, P. Moin, Approximate wall boundary conditions in the large-eddy simulation of high Reynolds number flow, Flow Turbul. Combust. 63 (2000) 269–291.
[35] X.X. Yu, C.G. Huang, T.Z. Du, L.J. Liao, X.C. Wu, Z. Zhi, Y.W. Wang, Study of characteristics of cloud cavity around axisymmetric projectile by large eddy simulation, J. Fluids Eng. 136 (2014) 051303.
[36] B. Stutz, J. Reboud, Experiments on unsteady cavitation, Exp. Fluids 22 (1997) 191–198.